# Passive acoustic localisation of undersea gas seeps using beamforming

Jianghui Li[a,*], Paul R. White[a], Jonathan M. Bull[b], Timothy G. Leighton[a], Ben Roche[b], John W. Davis[b]

[a] *Institute of Sound and Vibration Research, University of Southampton, Southampton SO17 1BJ, U.K.*
[b] *Ocean and Earth Science, University of Southampton, National Oceanography Centre, Southampton SO14 3ZH, U.K.*

**Abstract**

Passive acoustics has been identified as an important strategy to determine underwater gas flux at natural sites, or at locations related to anthropogenic activities. The ability of an acoustic system to detect, quantify and locate a gas leak is fundamentally controlled by the Signal to Noise Ratio (SNR) of the bubble sounds relative to the ambient noise. This work considers the use of beamforming methods to enhance the SNR and so improve the performance of passive acoustic systems. In this work we propose a focused beamforming technique to localise the gas seeps. To achieve high levels of noise reduction an adaptive beamformer is employed, specifically the minimum variance distortionless response (MVDR) beamformer. The technique is demonstrated using an array of five hydrophones collecting data at the controlled $CO_2$ gas release experiment conducted as part of STEMM-CCS (Strategies for Environmental Monitoring of Marine Carbon Capture and Storage) project. The experimental results show that the adaptive beamformer outperforms the conventional (delay and sum) beamformer in undersea bubble localisation. Furthermore, the results with a pair of hydrophone arrays show an improvement of the localisation compared to the use of one hydrophone array.

*Keywords:* `Beamforming, underwater acoustics, greenhouse gas, CO2, bubble, Marine Carbon Capture and Storage, CCS`

## 1. Introduction

Since 1850 the concentration of atmospheric greenhouse gas has more than doubled, with $CH_4$ mixing ratio increasing from 715 ppb in 1850 to 1875 ppb in 2020 and with the $CO_2$ mixing ratio increasing from 280 ppm in 1850 to 410 ppm in 2020, and these ratios continue to grow Szulejko et al. (2017). The increase of greenhouse gas in the atmosphere has resulted in global warming and the consequent change in the climate, which poses a serious threat to the habitability of the planet. In 2019, human activity resulted in 37 billion tons of $CO_2$ emissions into the atmosphere. To mitigate the impact of such anthropogenic $CO_2$, marine Carbon dioxide Capture and Storage (CCS) has been identified as an important strategy, which aims to permanently lock $CO_2$ in sub-seabed geological reservoirs Pachauri et al. (2014); Roelofse et al. (2019); Caserini et al. (2017); Vielstädte et al. (2019).

The risk management of the marine CCS strategies requires monitoring of the storage site to ensure its integrity Loewen and Melville (1991); Leighton and White (2011); Blackford et al. (2015); Mabon et al. (2014); Hvidevold et al. (2016); Berges et al. (2015); Atamanchuk et al. (2015); Taylor et al. (2015); Cevatoglu et al. (2015); Shitashima et al. (2015); Kolster et al. (2018); Stork et al. (2018); Kita et al. (2015). Consequently, effective monitoring techniques are urgently required. Recent technology developments for such monitoring include innovative methods in terms of acoustics, imaging, optics, chemistry, biology and geophysics Shitashima et al. (2015); Li et al. (2019b,a); Jenkins et al. (2012); Stalker et al. (2012); Zoback and Gorelick (2012); Johnson et al. (2009); Roberts et al. (2017). Acoustics is a key technology to achieve this, with roles for both active Nikolovska et al. (2008); Leblond et al. (2014); Leifer and Tang (2007); von Deimling et al. (2011) and passive Berges et al. (2015); Li et al. (2019a) methods. Both approaches have been used to understand gas seeps in the seabed subsurface and in the water column, and complement each other with active methods being effective as surveying tools for detecting and localising gas in the water

*Corresponding author: Jianghui Li

column, and passive techniques being well suited to long-term monitoring of small areas, providing estimates of gas flux and bubble size distributions von Deimling et al. (2010); Hovland and Sommerville (1985).

Beamforming is a fundamental signal processing method by which data from an array of sensors are combined to create a system with a directional response. This directivity provides two inter-related benefits: it increases the SNR and provides information about the location of a source. It achieves spatial selectivity by combining elements in a sensor array in such a way that signals at particular angles experience constructive interference while others experience destructive interference Li and Zakharov (2018). Such a technique has been used in radar, sonar, seismology, wireless communications, radio astronomy, acoustics and biomedicine. There is a wide range of array processing methods which have been developed, some of which only seek to solve the localisation problem (usually in the form of estimating the direction of arrival (DOA) of a signal) and other methods which seek to enhance the SNR and also allow localisation Li and Zakharov (2018); Li et al. (2016); Li (2017). Methods in the first group tend to be based on an eigen decomposition of the data correlation matrix and include techniques such as Multiple Signal Classification algorithm (MUSIC) and its many variants Schmidt (1979, 1986); Speiser (1986); Barabell (1983). The most familiar techniques which facilitate the enhancement of a signal alongside localisation are the Conventional Beamformer (CBF) and the Minimum Variance Distortionless Response (MVDR) beamformer (also referred to as a Capon beamformer) Capon (1969). The MVDR beamformer adjusts its response to minimise contamination from surrounding noise sources, so potentially offers greater improvements in SNR and higher resolution than CBF Capon (1969); Alexander (1986). However, the MVDR approach tends to perform less well in low SNR conditions and its performance can degrade significantly in the presence of modelling errors (e.g. inaccurate sensor locations).

In previous studies, a single hydrophone attached to an acoustic recorder has been used to measure the sounds of bubbles emerging from the seabed Li et al. (2019a), including in controlled gas release experiments, e.g. the QICS (Quantifying and Monitoring Potential Ecosystem Impacts of Geological Carbon Storage) project conducted off the west coast of Scotland Berges et al. (2015); Blackford et al. (2014), and natural gas seep sites Li et al. (2019a); Leifer and Tang (2007). However, SNR for single hydrophone installations can be low owing to underwater background noise Li et al. (2019b), e.g. ship noise and sea surface noise. Leighton and White Leighton and White (2011) proposed that an array of hydrophones, combined through a beamformer, can be used to increase the SNR of measurements and to locate the sources.

In this paper, we proffer and investigate a bubble focused beamforming method as a passive acoustic technique applied to the undersea gas seeps localisation. The proposed beamforming processes broadband bubble sound data based on the MVDR algorithm and the cross-spectral density matrix (CSDM). The effectiveness of the method is demonstrated using data collected during the controlled gas release experiment associated with the project STEMM-CCS (Strategies for Environmental Monitoring of Marine Carbon Capture and Storage `http://www.stemm-ccs.eu/`) in the central North Sea. In the experiment, a pair of hydrophone arrays with each comprising five hydrophones were deployed in a water depth of 120 m on the seafloor to collect the sound data associated with the gas bubble release. The proposed beamforming is compared to conventional beamforming and its ability to localise the bubble sound sources is investigated using data collected by a pair of hydrophone arrays.

The paper is organized as follows. We introduce the experimental configuration and data collection in Section 2. Section 3 presents the bubble focused conventional beamforming and the bubble focused MVDR beamforming. The localisation results using both broadband beamforming techniques are reported in Section 4. Discussion is drawn in Section 5, and conclusions are drawn in Section 6.

## 2. Experiment and hydrophone array deployment

This section describes the passive acoustic package of the STEMM-CCS controlled gas release experiment, and the deployment of the hydrophone arrays.

### *2.1. STEMM-CCS Experiment*

The central North Sea, which has been identified as the location of potential CCS sites Strachan et al. (2011); Shell (2017), provides an ideal site to conduct marine CCS experiment. The STEMM-CCS controlled

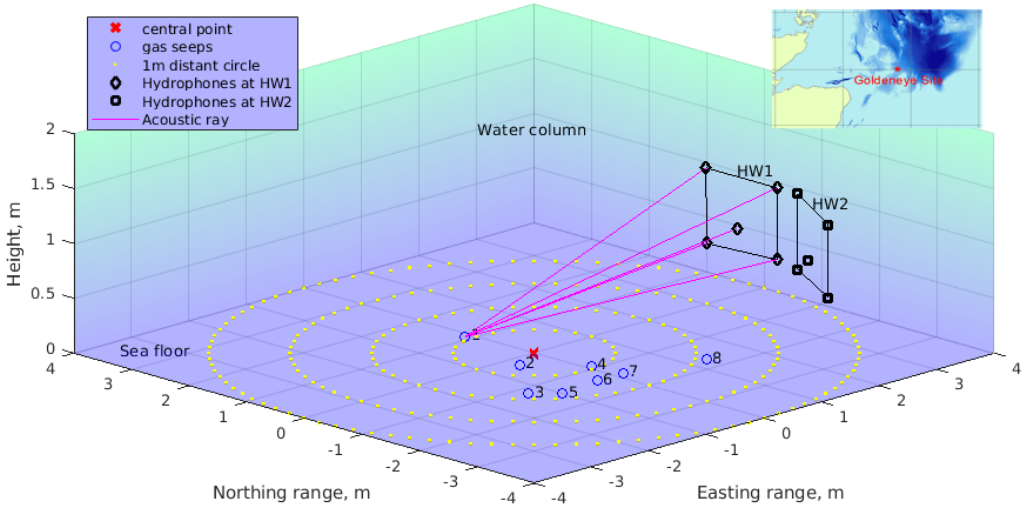


Figure 1: Experimental scenario with observed gas seep locations and hydrophone array locations at depth of 120 m in the central North Sea. The central red cross indicates the point above the tip of the gas diffuser; small blue circles on the seafloor represent eight optically observed gas seeps; the two hydrophone walls were separately placed at 3.3 m east from the central point; the acoustic rays from one seep to one hydrophone array are shown as an example; and dashed yellow circle lines are marked at 1 m intervals. The $CO_2$ gas injection rate varied between 0 and 143 kg/day.

gas release experiment was completed between 500 and 1000 m south-east of the Goldeneye platform Flohr et al. (2021a), around 100 km east of Scotland. To test the applicability of a variety of gas leakage monitoring techniques, we conducted a controlled sub-seabed $CO_2$ gas release experiment to replicate realistic leakage of gas that has migrated into the seabed environment. Directional drilling took place to insert a curved pipe, tipped with a gas diffuser, so that the pipe end was 4 m beneath the seafloor in a water depth of 120 m. $CO_2$ gas was injected into the overlying unconsolidated sediments, over a 5-week period, during which the flow rate was increased from 0 to 143 kg/day (50 L/min at STP) Flohr et al. (2021a); Li et al. (2021). The temporal and spatial behaviour gas seeps generated at the seafloor due to the injection were monitored using hydrophone arrays close to the gas injection site.

At the highest release rate, 143 kg/day, eight seeps with moderate and relatively high flow rates Flohr et al. (2021a) were optically observed by underwater cameras and acoustically recorded (Figure 1). In general, gas release paths, from the sub-seabed to the seafloor, can be complex. Furthermore, they can be influenced by numerous chemical/biological/physical factors. Consequently, it is possible for seeps to release gas into the water column only intermittently, even in periods when the mass flux injection rate into the sediment is constant. The hydrophone walls (see Figure 2(a)) were positioned using a Remotely-Operated-Vehicle (ROV) at a distance of 3.3 m east of the point which is directly above the gas diffuser (Figure 1).

The data used here were collected when the gas injection flow rate was 143 kg/day on 19$^{th}$ and 20$^{th}$ May 2019. At the seep site, ebullition occurred from a seabed mainly composed of silt, in a water depth of 120 m, when the temperature close to the seafloor was 7.7°C. Visual observation of the eight small seeps showed that each seep hole had a radius between 1 and 10 cm (see Figure 2(b)). The beamforming techniques used to localise the bubble sound sources associated with these seeps are based on the acoustic data recorded by hydrophones fixed on the hydrophone walls (HWs).

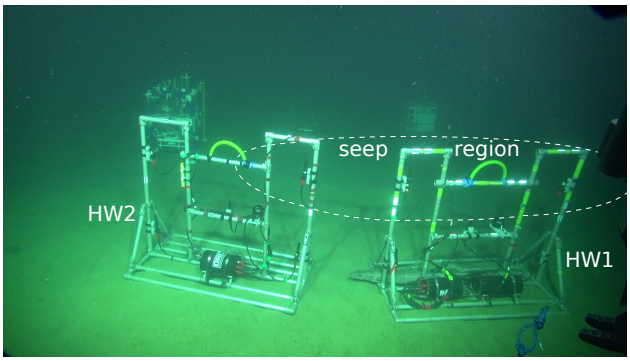


(a) 2 hydrophone walls

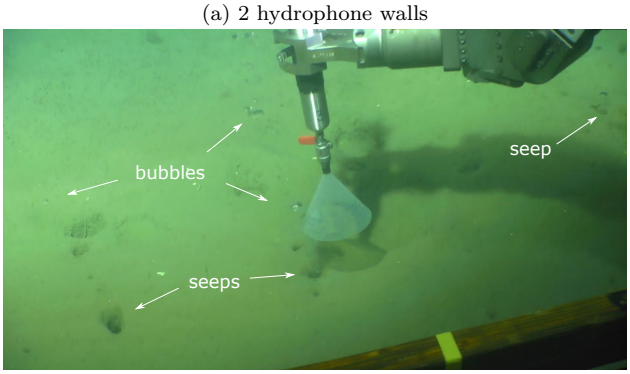


(b) seeping bubbles

Figure 2: Photographs showing (a) the two hydrophone walls (HWs) positioned on the seafloor, with the right one HW 1 and the left one HW 2, in front of which is the seep region circled by dashed line; (b) $CO_2$ bubbles emerging from small seabed depressions.

### *2.2. Hydrophone array deployment*

Figure 3 shows the schematic drawing of a hydrophone wall. Five hydrophones (Geospectrum M36, *GTI*) were linked to the acoustic recorder (RS-ORCA Multi-Channel Passive Acoustic Recorder, *RS Aqua*) (see Figure 2(a)), which were used to record the sound of bubbles escaping from the seabed. These hydrophones were absolutely calibrated for this water depth and temperature with receive sensitivity of -164.5 dB re: 1 V/$\mu$Pa. Each of the channels was sampled at 96 kHz, after a gain of 15 dB was applied. The passive system was programmed to make measurements at predetermined time intervals of 5 mins on and 5 mins off.

The hydrophones were arranged as a vertically oriented planar array, with roughly 0.6 m vertical aperture and 1.2 m horizontal aperture, see Figure 3 for precise details. The compact design was necessary to allow deployment and positioning of the arrays using an ROV. Further, the use of a planar configuration, in proximity to the source, allowed estimates of locations in the 3 dimensions to be formed. The use of such a planar array does not eliminate all ambiguities, there remains a front-back ambiguity that the array cannot resolve. Specifically, one cannot, from the acoustics alone, determine whether a source is in front or behind the array. However, video survey data collected by the ROV confirmed that there was no source of bubbles to the rear of the array.

## 3. Bubble acoustic focused broadband beamforming techniques

When a bubble is released from seafloor, sound is emitted. This acoustic signature arises as a consequence of the energy released when the buoyancy force overcomes the surface tension holding the bubble to the

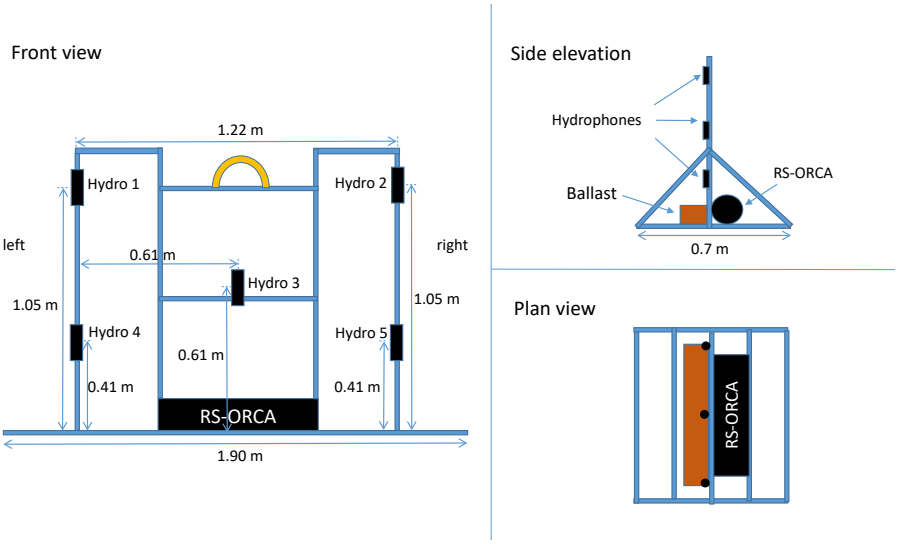


Figure 3: Schematic drawing of a hydrophone wall, comprising five hydrophones and an acoustic recorder (*RS-ORCA*); see *in situ* photograph in Figure 2(a).

seafloor Huh et al. (2013); Liu et al. (2017). This results in shape oscillations, including oscillations in the bubble's volume, which efficiently radiate sound Dziak et al. (2018); Chapman and Plesset (1971); Leighton and Walton (1987). The resulting signature is a transient sound approximating the shape of a damped sinusoid Keller and Kolodner (1956). The frequency of the oscillation relates to the bubble's volume and the damping coefficient is determined by a variety of factors Leighton (1994). During this experiment the duration of these sounds were observed to be typically around 15 ms and their centre frequencies lay in the range 1 to 10 kHz. These sounds are associated with the bubble formation process, so they are only generated in close vicinity of the seafloor. To illustrate, a typical bubble rise speed is 20 cm/s Clift et al. (2005), so the sound emission is completed whilst the bubble is within the first 3 mm of water above the sediment. Bubbles which receive no further excitation will rise silently above that height. However, processes such as fragmentation and coalescence can cause additional excitation, and may result in sounds being generated higher in the water column. Such processes will be more common in energetic gas releases, where many bubbles are formed simultaneously and interact with one another. For the input gas fluxes used in this experiment, bubbles were formed at a low rate and interactions appeared to be rare.

The sounds emitted by bubbles tend to have relatively low energy compared to the ambient noise, so that when observed at distances of a few metres each event is at a comparatively low Signal to Noise Ratio (SNR). Before localising the sound through beamforming, we first detected the individual bubble sounds. This was achieved using the method described in Li et al. Li et al. (2021). The data around each identified event was band pass filtered (1 – 10 kHz) and windowed (15 ms), and then was stored. This created a 15 ms data package containing a bubble signature as recorded on each of the 5 hydrophones in the array. Each data package was then processed using the different beamforming methods to localise the source of the sound. This process is illustrated in Figure 4.

During the time that this data was collected, there were 8 seeps sites observed using a camera mounted on a remotely operated vehicle. The experiment was conducted in a water depth of 120 m, so that acoustic reflections from the sea surface are negligible. The effect of the seabed on propagation is considered in Appendix A.

Two beamforming methods are considered for localising the sources Van Veen and Buckley (1988). The proximity of the array to the source of the sound (the bubbles) means that the far-field assumption prevalent in many applications of beamforming was not appropriate here. Therefore, the methods employed are what is sometimes called a focused beamformer, specifically methods which are designed to operate under near-field

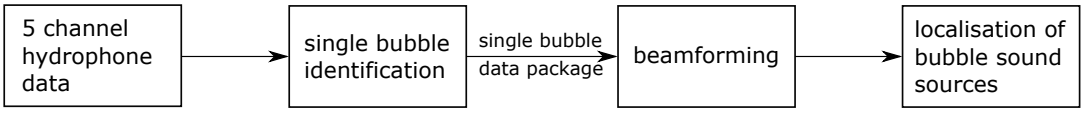


Figure 4: Block diagram of the approach used to localise single bubble sound sources.

conditions.

### *3.1. Broadband Conventional Beamformer (CBF)*

A CBF, also known as a delay-and-sum beamformer, is a widely used array processing technique Van Veen and Buckley (1988); Murino et al. (1994); Sutton (1979); Ferguson (1989); Pillai (2012); Johnson and Dudgeon (1993) which works by compensating for signal delays to each hydrophone appropriately before they are added together. The outcome of this delayed signal summation is a reinforced version of the signal emanating from the specified location.

In the near field of the hydrophone array, the wave front of the incident sound on the array is assumed to be spherical. Consider $N$ gas seeps radiating bubble sound received by $M$ omni-directional hydrophones, in which each hydrophone output is an attenuated and delayed version of the sound of a bubble from one of the seeps. On occasions the sounds from two bubbles will overlap in time and such data package will tend to generate spurious results. The damped oscillations of the bubble pulsation have a finite, but relatively narrow, bandwidth. Analysis is conducted in the frequency domain, so that after a Fourier transform is applied, a set of, $I$, frequencies, $f_i$, in the band $[f_{\text{start}}, f_{\text{end}}]$ are processed. For a signal, originating from the $n^{\text{th}}$ seep, measured on the $m^{\text{th}}$ hydrophone denoted, $b_{m,n}(f_i)$, can be expressed, for a frequency, $f_i$, as:

$$b_{m,n}(f_i) = s_n(f_i)h_{m,n}(f_i), \tag{1}$$

where $s_n(f_i)$ is the signal from the $n^{\text{th}}$ seep, and $h_{m,n}$ represents the effect of propagation from the $n^{\text{th}}$ seep to the $m^{\text{th}}$ hydrophone. $h_{m,n}$ is expressed relative to a reference sensor, herein taken as sensor 1, such that

$$h_{m,n}(f_i) = a_{m,n}e^{j2\pi f_i \tau_{m,n}}, \tag{2}$$

where $a_{m,n}$ is the attenuation factor, relative to the reference hydrophone:

$$a_{m,n} = \frac{d_{1,n}}{d_{m,n}}, \tag{3}$$

in which $d_{m,n}$ is the Euclidean distance from the $n^{\text{th}}$ seep to the $m^{\text{th}}$ hydrophone. The delays $\tau_{m,n}$ are defined as:

$$\tau_{m,n} = \frac{d_{m,n} - d_{1,n}}{c}, \tag{4}$$

where $c$ is the speed of sound underwater, assumed to be constant, and measured during the experiment as 1484 m/s. Note these delays can be positive or negative depending on the geometry of the problem and on the choice of reference hydrophone.

The measured hydrophone signals can be arranged into a $(M\times1)$ column vector, $\mathbf{X}(f_i)$, which can be expressed as:

$$\mathbf{X}(f_i) = \sum_{n=1}^{N} \mathrm{s}_n(f_i)\mathbf{h}_n(f_i) + \mathbf{V}(f_i) = \mathbf{H}(f_i)\mathbf{S}_n(f_i) + \mathbf{V}(f_i), \tag{5}$$

where $\mathbf{h}_n(f_i)$ is the $(M\times1)$ column vector, with elements defined in (2), called the steering vector, representing the propagation factors for the $n^{\text{th}}$ seep to each of the $M$ hydrophones. These steering vectors are

concatenated to form the $(M \times N)$ matrix $\mathbf{H}(f_i)$. $\mathbf{V}(f_i)$ corresponds to the $(M \times 1)$ noise vector the elements of which are the additive noise measured on the $m^{\text{th}}$ hydrophone.

CBF uses the steering vector as the weights to form the beamformer output, $y(f_i)$, as follows

$$y(f_i) = \sum_{m=1}^{M} x_m(f_i) h_{m,n}(f_i)^\star = \mathbf{h}(f_i)^H \mathbf{X}(f_i), \tag{6}$$

in which $\{\cdot\}^\star$ represents conjugation and $\{\cdot\}^H$ is the Hermitian transpose, $x_m(f_i)$ is the signal on the $m^{\text{th}}$ sensor, i.e. the $m^{\text{th}}$ element of $\mathbf{X}(f_i)$. The power at the output of the CBF is defined as

$$\mathrm{P}_{\mathrm{CBF}}(f_i) = \mathrm{E}\big[|y(f_i)|^2\big] = \mathbf{h}(f_i)^H \mathbf{Q}(f_i)^H \mathbf{h}(f_i) \tag{7}$$

where $\mathrm{E}\big[\,\cdot\,\big]$ is the expectation operator and $\mathbf{Q}(f_i)$ is defined by

$$\mathbf{Q}(f_i) = \mathrm{E}\big[\mathbf{X}(f_i)\mathbf{X}(f_i)^H\big]. \tag{8}$$

To obtain an estimate of $\mathbf{Q}$, the data packet is subdivided into shorter segments. Each of the $K$ subdivision provides an value of $\mathbf{X}_k(f_i)$. By averaging the outer product of these vectors with themselves, an estimate of $\mathbf{Q}(f_i)$ can be constructed:

$$\mathbf{Q}(f_i) = \frac{1}{K} \sum_{k=1}^{K} \mathbf{X}_k(f_i) \mathbf{X}_k{}^H(f_i) + \kappa \mathbf{I}_M, \tag{9}$$

where $\mathbf{I}_M$ is the $(M \times M)$ identity matrix, and $\kappa$ is a regularisation constant (here a value of $10^{-8}\mathrm{trace}\{\mathbf{Q}(f_i)\}/M$ is used). The choice of the number of segments $K$ involves a compromise where a larger values of $K$ results in fewer frequency bins (potentially poor resolution) but a lower variance in the estimate of $\mathbf{Q}(f_i)$. In this instance the measurement vectors are constructed by dividing the data package in to 16 segments of approximately 1 ms each.

The total power across the frequency band of interest, $P_{\mathrm{tot,CBF}}$, is computed by summing the powers at individual frequencies:

$$\mathrm{P}_{\mathrm{tot,CBF}} = \sum_{i=1}^{I} \mathrm{P}_{\mathrm{CBF}}(f_i). \tag{10}$$

### *3.2. Broadband MVDR (Minimum Variance Distortionless Response) beamformer*

As an adaptive beamforming, the MVDR beamformer mitigates the effect of the noise by minimizing the the overall output power whilst maintaining unit gain in the direction of the source Li and Zakharov (2018); Capon (1969); Alexander (1986); Cox and Zeskind (1992). The output of the beamformer can be expressed as:

$$y(f_i) = \sum_{m=1}^{M} w_m^\star x_m(f_i) = \mathbf{w}^H \mathbf{X}(f_i), \tag{11}$$

which is a generalization of (6) in which $\mathbf{w}$ is the vector of beamformer weights. In MVDR the weights are selected, via a constrained optimisation process, to minimise the output power, whilst maintaining unit gain for the assumed source location. The optimisation yields a well-known expression for the weights Capon (1969)

$$\mathbf{w} = \frac{\mathbf{Q}(f_i)^{-1}\mathbf{h}(f_i)}{\mathbf{h}(f_i)^H \mathbf{Q}(f_i)^{-1}\mathbf{h}(f_i)}, \tag{12}$$

from which the power of the MVDR output, $\mathrm{P}_{\mathrm{MVDR}}(f_i)$, can be expressed as:

$$\mathrm{P}_{\mathrm{MVDR}}(f_i) = \frac{1}{\mathbf{h}(f_i)^H \mathbf{Q}(f_i)^{-1} \mathbf{h}(f_i)} \tag{13}$$

In direct parallel to (7) the total power is obtained by summing (13) across all frequencies in the band of interest. One important practical issue associated with using MVDR processing is the computation of the inverse of the CSDM. To ensure that the approximation (13) is well conditioned, one rule of thumb is to ensure that $K > 2M$ Somasundaram (2011), in this instance we are using a $K$ of 16 with $M$ equal to 5, so this recommendation is exceeded.

For both CBF and MVDR the localisation problem is simplified since it is known that the sources of interest will only emit sounds close to the seafloor in front of the array. The localisation process divides the seafloor into a regular grid of points. The spacing in the grid corresponds to the approximate size of a release point, specifically the grid points are separated by 25 cm. The power of the signal estimated to have emanated from each grid point can be computed using each of the beamforming methods, to construct a 2D surface of signal power as a function of location. Peaks in this surface are expected to correspond to seep sites and for every data package one can find the highest peak in the surface and its location is used as an estimate for the location of the source of that bubble sound.

## 4. Experimental results

This section presents the results from the two localisation methods (see Section 3), comparing those localisations to position estimates obtained from optical data collected during the STEMM-CCS experiment (see Section 2.1). Further, the effect of combining data from a second asynchronous array is considered.

Analysis of some sections of the data are shown in Figure 5. Figure 5(a) compares power spectral densities (PSDs) under two conditions. One data set, collected on 9$^{\mathrm{th}}$ May 2019, during a period when there were no research vessels on-site, prior to the start of gas injection (gas flux 0 kg/day). This shows a relatively featureless PSD representing the ambient noise conditions. The second data set was collected during 20$^{\mathrm{th}}$ May 2019, when the gas injection rate was at its maximum (143 kg/day) with the research vessels holding station at a distance of >1 km from the release point. This curve shows high frequency noise above 8 kHz, where the noise comes from pumps used another experimental lander on the site. At lower frequencies, there are some small peaks which are noise from the bow thrusters of the distant research vessel as it holds station.

### *4.1. Single bubble selection*

Figure 5(b) shows the spectrogram of 4 s data as an example of data measured by a single hydrophone (the central hydrophone, number 3) during the experiment at the gas injection rate 143 kg/day. Whilst Figure 5(c) shows the cross-spectrogram computed for the same period using the data from all of the hydrophones. The bubbles are identified using the method described in Li et al. (2021) and the result is shown in Figure 5(d). These identified events reveal that bubbles are dominantly primarily located in the frequency interval 2 to 8 kHz at this depth, corresponding to bubble radii of about 5 to 1 mm.

### *4.2. Comparison of beamforming techniques*

This subsection considers the comparison of the two beamforming methods (Section 3) applied to the data packages containing bubble signatures. The resonance frequency of the bubble in each data packet is measured, the packets are then collected together in bins centred on $1, 2, 3, \ldots, 10$ kHz. Locations are estimated by computing the power associated with a set of points arranged in a uniform grid on the seafloor.

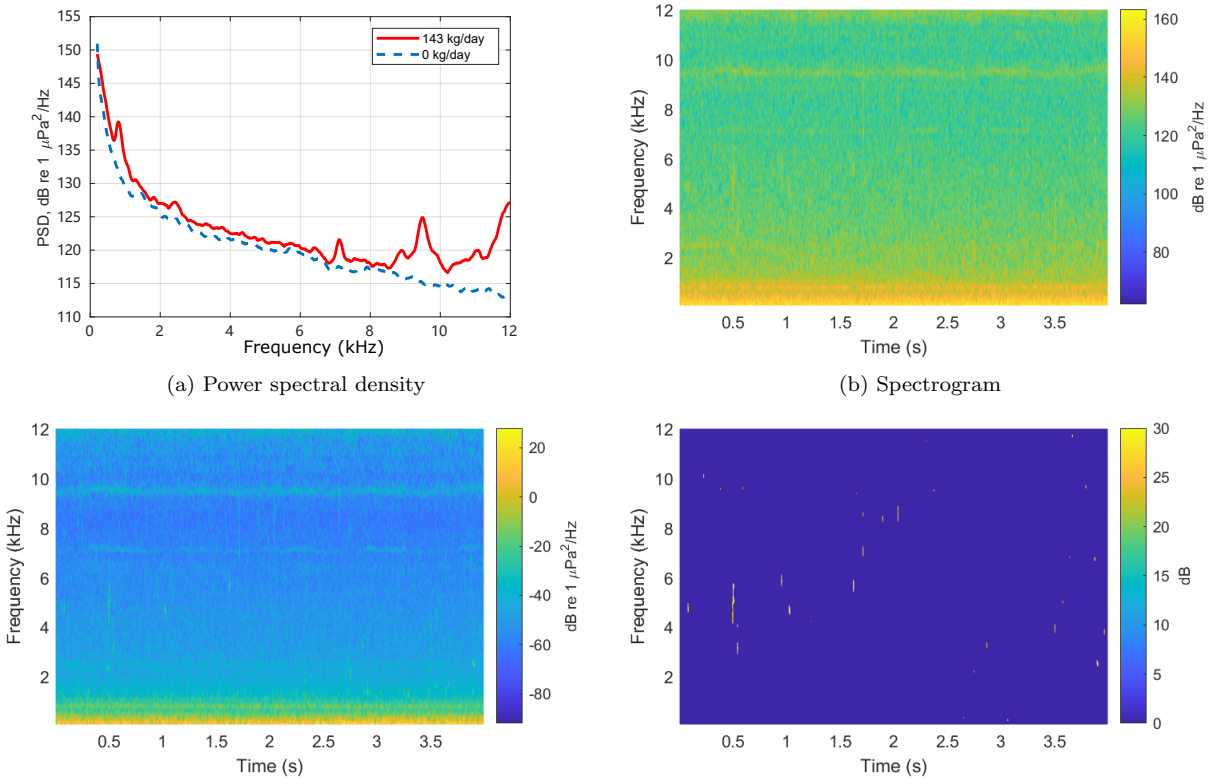


Figure 5: Power spectral density (PSD) and spectrogram of signals measured on a single hydrophone (number 3). (a) Comparison of PSD of the sound received at gas injection rates 143 kg/day (50 L/min) and 0 kg/day; (b) Spectrogram of 4 s of data from 143 kg/day condition; (c) Cross-spectrogram of the array data; (d) Detected bubble pulses (yellow dots) from cross-spectrogram, predominantly occurring in the band 2 to 8 kHz. (see online version for color figures)

#### *4.2.1. SNR (Signal to Noise Ratio) improvement*

Figure 6 shows comparisons of the data package waveforms received at hydrophone 3 (red), the CBF beamformed data package waveforms (blue) and the MVDR beamformed data package waveforms (black) at various frequencies between 2 kHz and 8 kHz. In all these cases, we can see that it is easier to identify the bubble signatures from the MVDR beamformed signals compared to that received directly by hydrophone channels, which reveals an improvement of the bubble SNR. The CBF only provides visible enhancement in 2 of the instances (Figure 6(b)&(d)). For these data, the bubble pulsation length is typically 15 ms, and the measured pressure amplitude is from 0.05 to 0.1 Pa in all four cases.

In order to assess the performance of the methods we compute the SNR before and after beamforming with the two techniques. To compute the SNR within a data package the signal is first bandpass filtered, to remove energy outside of the 1 to 10 kHz band. A 45 ms period centred on the detected bubble sound is identified. The middle 15 ms period, denoted $x_u(t)$, is assumed to correspond to the bubble sound whilst the 15 ms periods before and after the bubble, denoted $\nu_u(t)$, are assumed to noise. The SNR is then computed based on the signal powers in these windows. Those powers are then averaged across a total of $U$ bubbles. To allow further insights the bubbles are collected together in 1 kHz bins based on their centre frequency, and the SNRs are computed for bubbles of different centre frequencies using those bins. This does mean that $U$ varies for each frequency bin, but in all cases more than 100 bubbles are employed to compute the

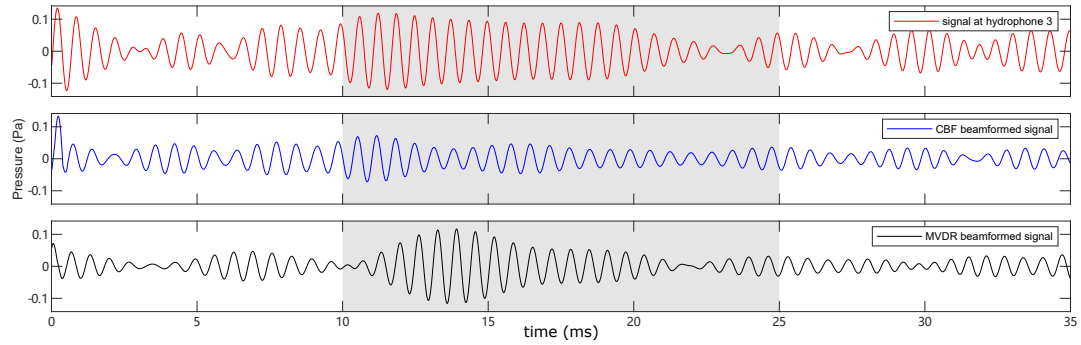


(a) 2 kHz

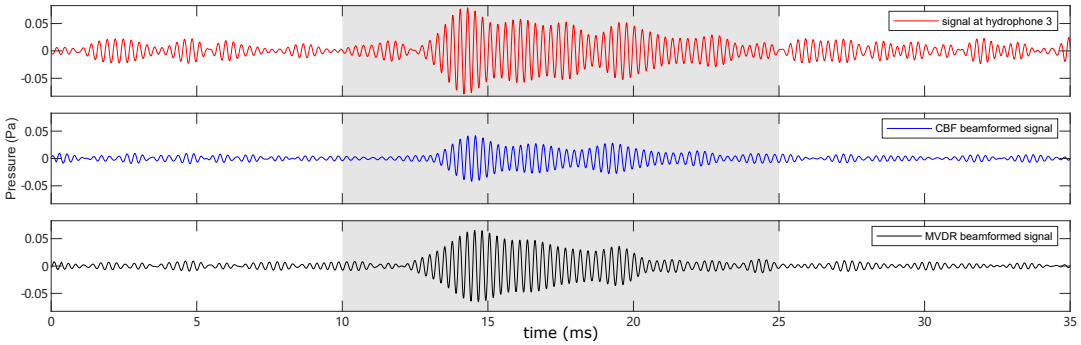


(b) 4 kHz

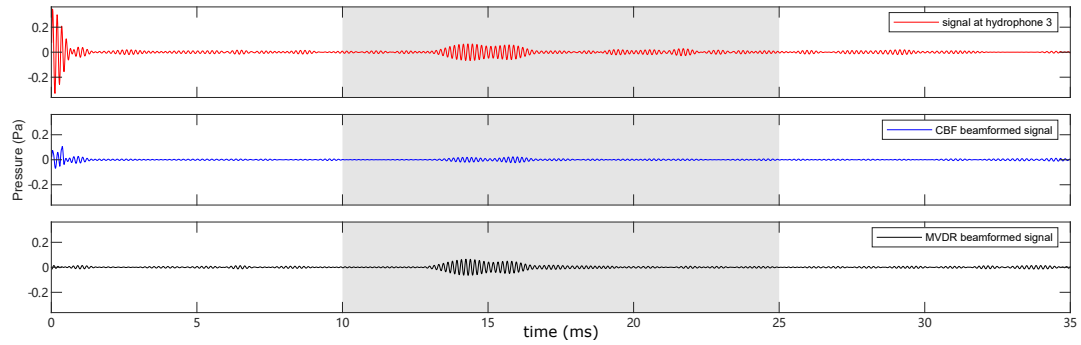


(c) 6 kHz

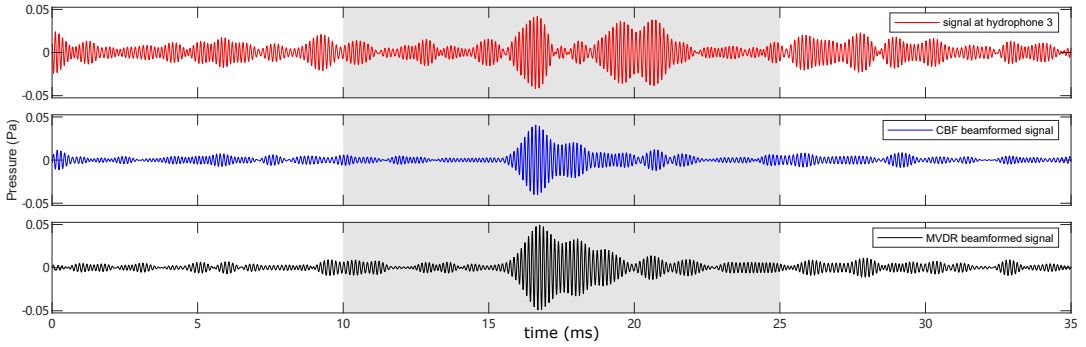


(d) 8 kHz

Figure 6: Comparison of acoustic signal waveforms received at hydrophone 3 (red) and beamformed signals (CBF in blue and MVDR in black) at various frequencies: (a) 2 kHz; (b) 4 kHz; (c) 6 kHz; (d) 8 kHz. The grey region in these plots show the 15 ms window corresponding to the likely bubble location. In all cases, the bubble SNR has been improved by MVDR, while in some cases CBF does not show a clear SNR improvement.

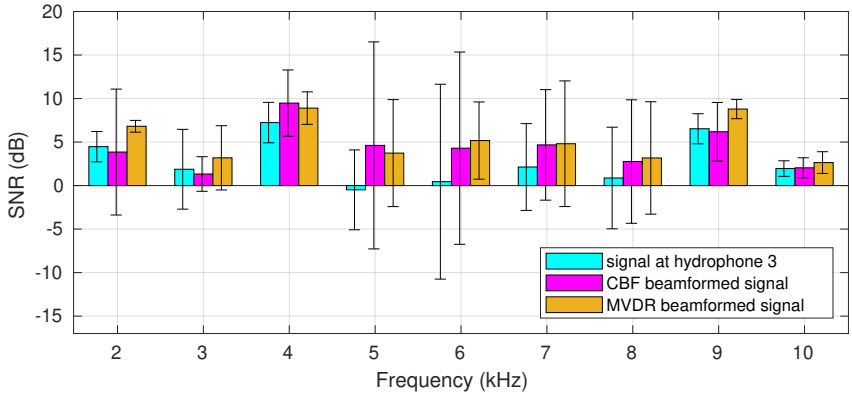


Figure 7: Bubble SNR for the two beamformer outputs and the raw hydrophone signals. Data is shown in 1 kHz frequency bins for the centre frequency of the bubbles. For MVDR beamforming, an average of 3 dB improvement of the SNR can be observed. The dominant resonance frequency of gas bubbles are from 5 to 8 kHz, showing the highest SNR improvement. The CBF beamforming does not show significant bubble SNR improvement.

SNRs. Accordingly, the SNR is computed according to:

$$\mathrm{SNR[dB]} = 10\log_{10}\left(\frac{\sum_{u=1}^{U}\sum_{t=1}^{T}\mathrm{x_u}(t)^2 - \sum_{u=1}^{U}\frac{1}{2}\sum_{t=1}^{2T}\nu_\mathrm{u}(t)^2}{\sum_{u=1}^{U}\frac{1}{2}\sum_{t=1}^{2T}\nu_\mathrm{u}(t)^2}\right), \tag{14}$$

where $T$ is the number of samples in a 15 ms window.

Figure 7 shows the SNR computed for the unprocessed data received at hydrophone 3, the CBF beamformed data and the MVDR beamformed data. We can see that MVDR beamforming consistently enhances the SNR across the frequency range. It produces an average of a 3 dB improvement compared to the unprocessed data. The performance of CBF is considerably more variable, in two frequency bands (4 kHz and 5 kHz) the SNR improvement exceeds that of MVDR. The dominant resonance frequencies of gas bubbles are from 5 to 8 kHz, where the SNR improvement of MVDR is up to 5 dB (specifically at 6 kHz, the SNR improvement is from 0.5 to 5.5 dB). Further, the MVDR results are more consistent, showing lower variability, than those of the CBF in these frequency bands.

*4.2.2. Example of localisation*

Figure 8 shows examples of localisation results of four individual bubble data packages at resonance frequencies close to frequencies 2 kHz, 4 kHz, 6 kHz and 8 kHz, with the sub-figures in the left column showing the results for CBF with segmented data package processed ((9) into (7)); and those in the right showing the results for MVDR ((9) into (13)). The red star indicates the grid position with the highest power, denoting the identified sound source. Voronoi diagram Yap (1987); Wan et al. (2019) is added to each of the localisation maps, showing the boundary around a seep that includes all points closer to it than to any other seep.

The comparison of the performance of the two techniques for localisation is hampered by the lack of ground truth data: which of the eight potential sites is the actual source of a bubble sound is not known. Examination of Figure 8 illustrates some general trends, the estimated locations using CBF appear outside the cluster of known seep sites, with the exception of the 8 kHz case, contrasting with the MVDR estimates which are all within that cluster. In the absence of ground truth, the approach to measuring performance was to measure the distance between the estimated location and the nearest known seep location (the Voronoi diagrams allow the reader to more easily identify which seep is closest to the estimated location).

The higher sidelobes associated with the CBF are evident in Figure 8, appearing as multiple peaks away from the largest peak (the main lobe). These sidelobes have amplitudes close to that of the main lobe,

suggesting that small perturbations, for example due to noise, might generate large changes in the estimated locations. The sidelobes in the MVDR plots are generally lower implying a more robust solution.

#### *4.2.3. Analysis of localisation*

The localisation results in these cases described above reveal the effectiveness of the bubble sound source localisation by using the proposed bubble focused broadband MVDR beamforming. Here we statistically investigate the CBF and the MVDR applied on the collected data from HW 1. The average error, i.e. distances between estimated locations and the nearest seep, based on 1500 bubbles, is 1.32 m for estimated locations based on CBF; and is 0.94 m for estimated locations formed using MVDR. This indicates that MVDR possesses higher accuracy than CBF for seep localisation.

### *4.3. Comparison of array geometries*

In this experiment two sets of 5 hydrophones were deployed on two hydrophone walls. Within a hydrophone wall all 5 channels of data were sampled synchronously, but the two systems ran on separate internal clocks, so between the two walls the sampling was asynchronous. Consequently beamforming could be applied separately within each of the arrays, but the elements could not be combined to create a single larger array. This section explores effect of combining the data from these two systems to create a single estimate of source location.

Figure 9 shows the power distributions computed using MVDR applied to the two hydrophone walls individually and an estimate obtained by combining them. In Figure 9(a), the two HWs identify power peaks closer to each other, but HW1 identifies the bubble source closer to seep 8 with an error of 1.5 m and HW2 identifies the source closer to seep 4 with an error of 1 m. After the combination, the suggested seep location is one closer to seep 4 (with an error of about 1 m). In Figure 9(b)&(c), both cases identify the power peaks closest to seep 4. However, several other power clusters, side lobes, are visible in the left and middle plots with single HW used. The process of combining the data from the two systems serves to reduces these side lobes in all instances. This improves the robustness of the location estimates.

To statistically investigate the accuracy of the localisation with hydrophone walls, we analyse results from 1500 bubble data packages, as described in Section 4.2.3. The average MVDR localisation error from HW 1 alone is 0.94 m and from HW 2 the mean error is 0.84 m. While the error reduces to 0.76 m when data from both HWs are used. This confirms that the application of more hydrophone walls allows less localisation error of bubble seeps.

## 5. Discussion

This paper has considered some of the practical issues of detecting and localising bubbles sounds under real world conditions using an array of hydrophones. The challenge of detecting and localising the relatively quiet, transient, sounds associated with bubble formation has been considered using two established beamforming methods, CBF and MVDR. For this experiment the sources of sound comprised eight closely clustered seep locations where bubbles were being formed. The performance advantages offered by MVDR over CBF in idealised circumstances is well-established. However, in this experiment mismatches between the assumptions of the model underpinning MVDR and reality were anticipated, so its potential performance benefits might not be realised. The positioning errors for the acoustic centres of the hydrophones within the array were known roughly $\pm 1$ cm, the locations of the array and the hydrophone walls on the seafloor are estimated from video analysis, so are subject to some uncertainty. Additionally, the angular positions of the arrays is subject to uncertainty in all 3 directions (i.e. angles corresponding to pitch, roll and yaw).

The algorithms' performance was assessed using metrics based on signature of individual bubbles. Those bubbles are detected using a method described in a companion paper Li et al. (2021). The performance is assessed in terms of the enhancement of the SNR obtained through the use of the beamformers and the localisation accuracy. Both assessment methods are hindered by the lack of absolute ground truth data, whilst estimates of the locations of the seeps were available from video analysis, it was not possible to associate an individual sound with a specific seep location.

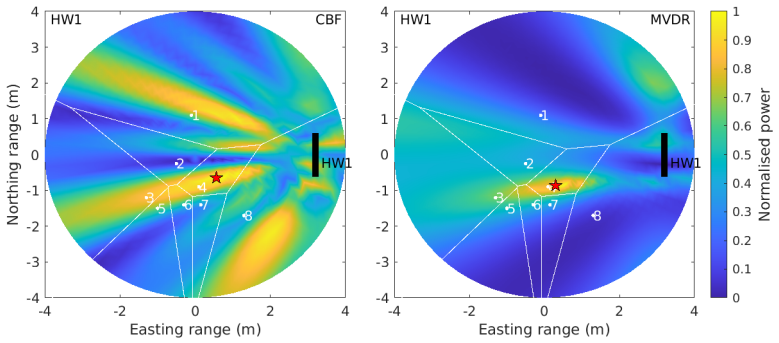


(a) 2 kHz

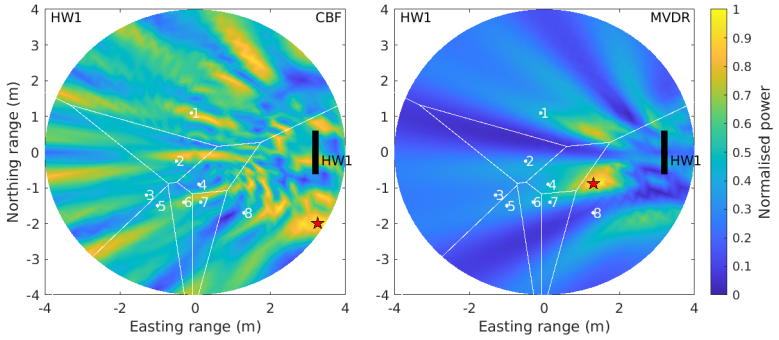


(b) 4 kHz

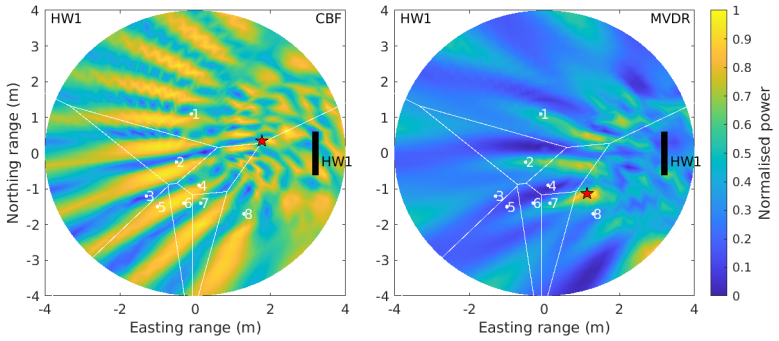


(c) 6 kHz

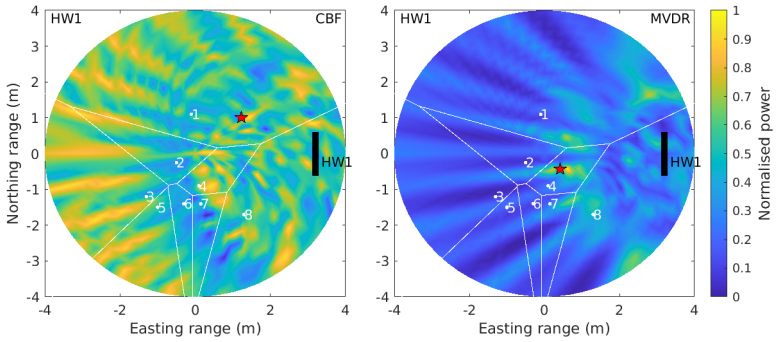


(d) 8 kHz

Figure 8: Comparison of CBF (left) and MVDR beamforming (right) for the localisation of single bubbles at various frequencies from separate 15 ms data samples. (a) 2 kHz; (b) 4 kHz; (c) 6 kHz; (d) 8 kHz. In all these cases, the MVDR beamforming outperforms the two CBFs with smaller error to each seeps in the Voronoi diagram. However, the CBFs always has a contribution near MVDR peak. Red stars indicates the grid with the highest normalised power (the power is normalised such that the maximum power is 1 and the minimum is 0).

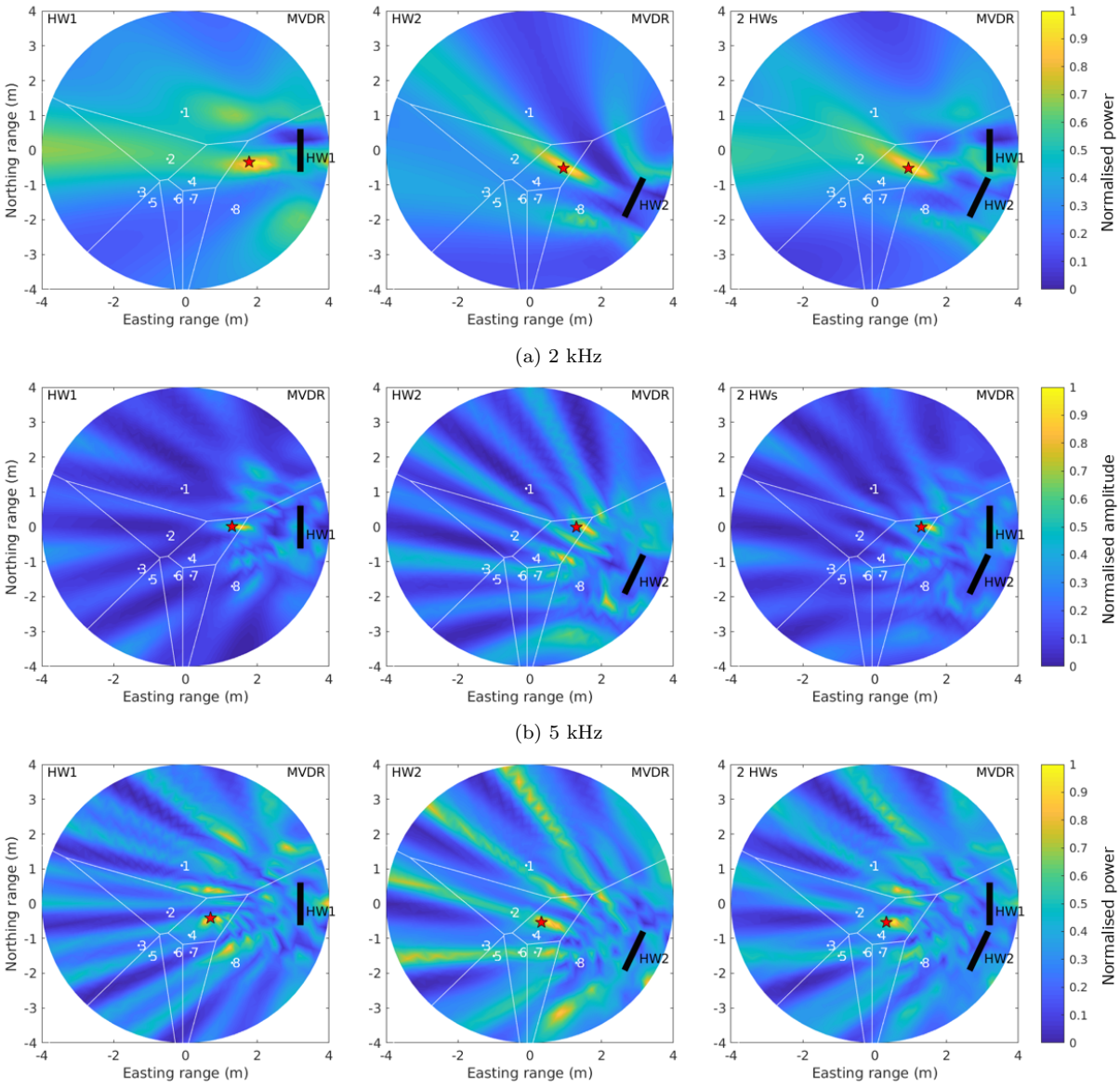


(a) 2 kHz

(b) 5 kHz

(c) 8 kHz

Figure 9: MVDR beamforming results with hydrophone wall 1 (HW 1), HW 2, and both HWs. The use of two HWs reduces uncertainty of the localisation. Voronoi diagram is used to show boundaries around which include all points closer to a gas seep than to any other gas seeps in the set. Red stars are localised bubble sound sources with the highest power amplitude.

The SNR improvement offered by the two beamformers was compared to than on a single hydrophone. The SNR was averaged across 1500 bubbles in total. At all frequencies MVDR did achieve a reasonable performance enhancement over a signal hydrophone, and at most frequencies it realised a performance advantage over CBF. The exact SNR gain one would predict using MVDR depends on the specific spatial distribution of noise in an environment, but one would anticipate a greater SNR gain that achieved for CBF, with the performance of MVDR being especially improved by the presence of noise sources focused in discrete locations. For CBF one predicts a maximum gain of 7 dB ($10\log_{10}(5)$): for a 5 element array, assuming an isotropic noise field and sensor spacing of $\lambda/2$, $\lambda$ being the wavelength of the incident sound. In this data one would not anticipate MVDR showing dramatic improvements relative to CBF since, in the band of interest, there are no noise sources which are spatially localised. The SNR gain realised is less than 7 dB, in some frequency bands, the maximum gain being around 5 dB using MVDR. On average the gains for MVDR is around 3 dB and is lower and rather inconsistent for CBF. It should be noted that SNR gain of 3 dB from beamforming means that an array can sense bubbles which are 40% further away than a single hydrophone can measure on its own. The SNRs gains measured fall short of 7 dB because a) the spacings between sensors are less than $\lambda/2$ at the lower end of the frequency range, b) close to the seafloor the sound field will not conform to an isotropic assumption and c) the various positional errors in the system.

The ability of the arrays to localise the sound sources quite limited because of the small aperture of the array and the distance to the source in comparison to that aperture. This problem is exacerbated at low frequency where the dimensions of the main lobe are large compared to those seen at higher frequencies (see Figure 8 for example). Similarly at higher frequencies large side lobes (not fully developed grating lobes) are evident. The large side lobes mean that small perturbations can cause large changes in the estimated source location. These side lobes are more in evidence in the CBF than in the MVDR (Figure 8). Without information about the seep giving rise to a particular bubble event, the estimate of location error is based on a measure: the distance to the nearest known seep site. This makes the measure less sensitive than it might otherwise be. However, using this metric MVDR achieves roughly a 30% reduction in error, measuring the location with a mean error of a little less than 1 m. Such an error is not sufficiently small to allow confident attribution of a single sound to a particular seep site. A second hydrophone wall was available and combining the data from the two walls yielded an error of 0.75 m. This is still of the same order as the spacing between the seeps, so whilst it improves localisation it does not allow confident attribution to a specific seep.

## 6. Conclusions

This paper has demonstrated the utility of beamforming as a tool for analysis of acoustic data from gas releases. It has shown that the MVDR beamformer offers worthwhile performance gains over CBF. Both in terms of greater enhancement of SNR and in terms of localisation accuracy. Whilst some localisation of sound sources was achieved, it was not possible to obtain an error smaller than that typical spacing between seeps, so whilst sounds could be located to the general area of the collection of seeps, location to a specific release point was not achievable. However, using beamforming it was possible to enhance the SNR and in so doing extend the range over which the passive acoustic system can detect and monitor a leak.

## Appendix A. Propagation loss modelling

To verify the appropriate assumption of spherical spreading of the bubble sounds propagation in the acoustic channel, we apply a propagation loss modelling. The sea state was primarily 3 and thus the sea surface is considered to be flat in the propagation channel modelling. The seabed is considered as an acousto-elastic half space without layers. In the Goldeneye area of the North Sea, the seafloor was covered with sand Flohr et al. (2021b) (Figure 2). Similar seabed sediment properties are used from reference Porter (1992); Jackson and Richardson (2007); Hamilton (1970); Hampton (1967) to define the parameters in our modelling, i.e. the chosen sound speed of the mud is 1520 m/s; the density of the sediment is taken to be 1.45 g/cm$^3$; and a bottom attenuation coefficient of 0.05 dB/wavelength is appropriate (Porter, 1992; Jackson and Richardson, 2007; Hamilton, 1970; Hampton, 1967). The measured SSP is shown in Fig. A.10(a). The bubble sound source is considered to be omnidirectional.

Typical underwater acoustic propagation channels contain characterised as multipaths, e.g. assumed to be reflections from the sea surface and seafloor, propagation in the seabed, and refraction in the water column due to the depth-dependent sound speed profile (SSP) Li et al. (2016); Li and Zakharov (2018); Li et al. (2018); Li (2017); Li et al. (2020). Thus a simplification of spherical spreading of the bubble sound radiated from the seafloor may not be accurate. While the dominant frequency for the bubble sound is relatively low (up to 10 kHz), here we apply the parabolic equation model as a proper model to simulate the propagation loss (Tappert, 1977; Li et al., 2019c). The code that we use for the simulation is a modified version of the software AcTUP presented in (Maggi and Duncan, 2005). It takes into account the SSP, bathymetry, and bottom properties as well as multipath acoustic propagation. With the measured SSP and estimated attenuation values, we run the parabolic equation to determine the propagation loss at the appropriate bubble sound source and hydrophone depth/range locations. The source depth is set to 120 m below the sea surface, i.e. on the seafloor.

Figure A.10(b) shows the estimated propagation loss as a function of depth and range, which is influenced by the SSP. Specifically, we choose the depth of each hydrophone to calculate the propagation loss. Figure A.11 shows the propagation loss at different water depth of the hydrophones. It is shown that the assumption of spherical spreading is reasonable in our experimental conditions.

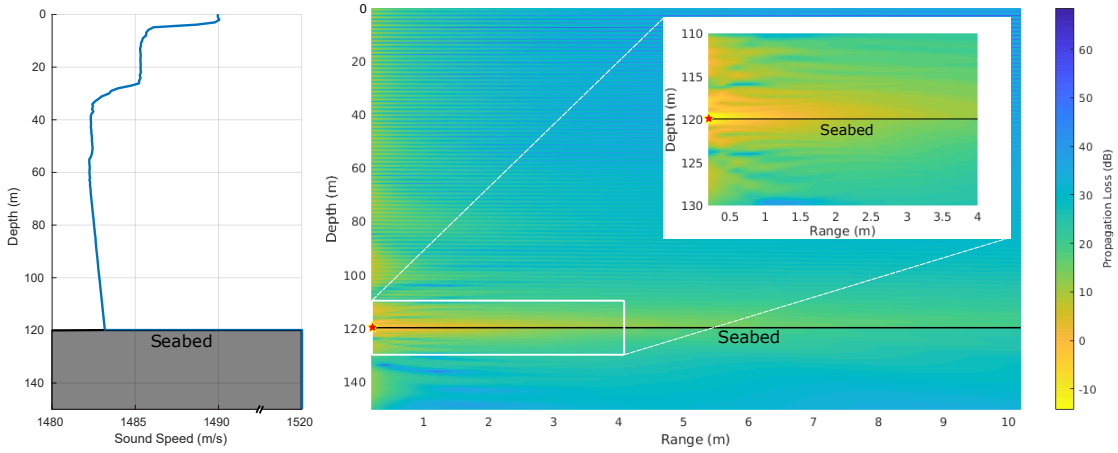


(a) Sound speed profile (b) Propagation loss

Figure A.10: Sound speed profile and propagation loss. (a) sound speed profile (SSP) measured at the experimental area in the central North Sea; (b) simulation of propagation loss performed at 1 kHz in the acoustic channel involving seabed subsurface and water column as the function of depth and range. The red star denotes a gas bubble seep at depth 120 m.

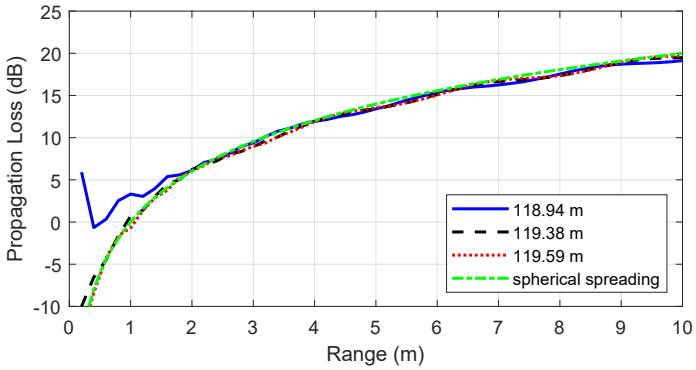


Figure A.11: Comparison of propagation loss calculation with the parabolic equation simulation considering geometry and spherical spreading at different water depth of the hydrophones on the Hydrophone Wall: 118.94 m of hydrophone 1, 119.38 m of hydrophone 3, and 119.59 m of hydrophone 4. These propagation losses are close to each other at ranges more than 2 m, indicating the considerable considering of spherical spreading in the main text.


## Acknowledgements

Funding was provided by the European Unions Horizon 2020 research and innovation programme under the grant agreement number 654462 (STEMM-CCS). We are grateful to the Captain of the RRS 'James Cook' and crew for enabling the scientific measurements at sea during the JC180 cruise.


## References


Alexander, S.T., 1986. Adaptive signal processing: theory and applications. Springer-Verlag New York, Inc. doi:10.1007/978-1-4612-4978-8.

Atamanchuk, D., Tengberg, A., Aleynik, D., Fietzek, P., Shitashima, K., Lichtschlag, A., Hall, P.O., Stahl, H., 2015. Detection of $CO_2$ leakage from a simulated sub-seabed storage site using three different types of $pCO_2$ sensors. International Journal of Greenhouse Gas Control 38, 121–134. doi:10.1016/j.ijggc.2014.10.021.

Barabell, A., 1983. Improving the resolution performance of eigenstructure-based direction-finding algorithms, in: ICASSP'83. IEEE International Conference on Acoustics, Speech, and Signal Processing, IEEE. pp. 336–339. doi:10.1109/ICASSP.1983.1172124.

Berges, B.J., Leighton, T.G., White, P.R., 2015. Passive acoustic quantification of gas fluxes during controlled gas release experiments. International Journal of Greenhouse Gas Control 38, 64–79. doi:10.1016/j.ijggc.2015.02.008.

Blackford, J., Bull, J.M., Cevatoglu, M., Connelly, D., Hauton, C., James, R.H., Lichtschlag, A., Stahl, H., Widdicombe, S., Wright, I.C., 2015. Marine baseline and monitoring strategies for carbon dioxide capture and storage (CCS). International Journal of Greenhouse Gas Control 38, 221–229. doi:10.1016/j.ijggc.2014.10.004.

Blackford, J., Stahl, H., Bull, J.M., Bergès, B.J., Cevatoglu, M., Lichtschlag, A., Connelly, D., James, R.H., Kita, J., Long, D., et al., 2014. Detection and impacts of leakage from sub-seafloor deep geological carbon dioxide storage. Nature climate change 4, 1011–1016. doi:10.1038/nclimate2381.

Capon, J., 1969. High-resolution frequency-wavenumber spectrum analysis. Proceedings of the IEEE 57, 1408–1418. doi:10.1109/PROC.1969.7278.

Caserini, S., Dolci, G., Azzellino, A., Lanfredi, C., Rigamonti, L., Barreto, B., Grosso, M., 2017. Evaluation of a new technology for carbon dioxide submarine storage in glass capsules. International Journal of Greenhouse Gas Control 60, 140–155. doi:10.1016/j.ijggc.2017.03.007.

Cevatoglu, M., Bull, J.M., Vardy, M.E., Gernon, T.M., Wright, I.C., Long, D., 2015. Gas migration pathways, controlling mechanisms and changes in sediment acoustic properties observed in a controlled sub-seabed $CO_2$ release experiment. International Journal of Greenhouse Gas Control 38, 26–43. doi:10.1016/j.ijggc.2015.03.005.

Chapman, R.B., Plesset, M.S., 1971. Thermal effects in the free oscillation of gas bubbles doi:10.1115/1.3425258.

Clift, R., Grace, J.R., Weber, M.E., 2005. Bubbles, drops, and particles .

Cox, H., Zeskind, R.M., 1992. Adaptive cardioid processing, in: IEEE Conference Record of The Twenty-Sixth Asilomar Conference on Signals, Systems and Computers., pp. 1058–1061. doi:10.1109/ACSSC.1992.269137.

von Deimling, J.S., Greinert, J., Chapman, N., Rabbel, W., Linke, P., 2010. Acoustic imaging of natural gas seepage in the north sea: Sensing bubbles controlled by variable currents. Limnology and Oceanography: Methods 8, 155–171. doi:10.4319/lom.2010.8.155.

von Deimling, J.S., Rehder, G., Greinert, J., McGinnnis, D., Boetius, A., Linke, P., 2011. Quantification of seep-related methane gas emissions at tommeliten, north sea. Continental Shelf Research 31, 867–878. doi:10.1016/j.csr.2011.02.012.

Dziak, R., Matsumoto, H., Embley, R., Merle, S., Lau, T.K., Baumberger, T., Hammond, S., Raineault, N., 2018. Passive acoustic records of seafloor methane bubble streams on the oregon continental margin. Deep Sea Research Part II: Topical Studies in Oceanography 150, 210–217. doi:10.1016/j.dsr2.2018.04.001.

Ferguson, B.G., 1989. Improved time-delay estimates of underwater acoustic signals using beamforming and prefiltering techniques. IEEE Journal of Oceanic Engineering 14, 238–244. doi:10.1109/48.29601.

Flohr, A., Matter, J., James, R., Lichtschlag, A., Peel, K., Pearce, C., Connelly, D., 2021a. Quantification of leakage from sub-seabed $CO_2$ storage using natural and added geochemical tracers. International Journal of Greenhouse Gas Control , to be presented.

Flohr, A., Schaap, A., Achterberg, E.P., Alendal, G., Arundell, M., Berndt, C., Blackford, J., Böttner, C., Borisov, S.M., Brown, R., et al., 2021b. Towards improved monitoring of offshore carbon storage: A real-world field experiment detecting a controlled sub-seafloor co2 release. International Journal of Greenhouse Gas Control 106, 103237. doi:10.1016/j.ijggc.2020.103237.

Hamilton, E.L., 1970. Sound velocity and related properties of marine sediments, North Pacific. Journal of Geophysical Research 75, 4423–4446. doi:10.1029/JB075i023p04423.

Hampton, L.D., 1967. Acoustic properties of sediments. The Journal of the Acoustical Society of America 42, 882–890. doi:10.1121/1.1910662.

Hovland, M., Sommerville, J.H., 1985. Characteristics of two natural gas seepages in the north sea. Marine and Petroleum Geology 2, 319–326. doi:10.1016/0264-8172(85)90027-3.

Huh, C., Jung, J.Y., Cho, M.I., Kang, S.G., 2013. A numerical study on $co_2$ seepage from offshore geologic storage site. Energy Procedia 37, 3432–3438. doi:10.1016/j.egypro.2013.06.232.

Hvidevold, H.K., Alendal, G., Johannessen, T., Ali, A., 2016. Survey strategies to quantify and optimize detecting probability of a $CO_2$ seep in a varying marine environment. Environmental Modelling & Software 83, 303–309. doi:10.1016/j.envsoft.2016.06.006.

Jackson, D., Richardson, M., 2007. High-frequency seafloor acoustics. Springer Science & Business Media.

Jenkins, C.R., Cook, P.J., Ennis-King, J., Undershultz, J., Boreham, C., Dance, T., de Caritat, P., Etheridge, D.M., Freifeld, B.M., Hortle, A., et al., 2012. Safe storage and effective monitoring of $CO_2$ in depleted gas fields. Proceedings of the National Academy of Sciences 109, E35–E41. doi:10.1073/pnas.1107255108.

Johnson, D.H., Dudgeon, D.E., 1993. Array signal processing: concepts and techniques. PTR Prentice Hall Englewood Cliffs.

Johnson, G., Raistrick, M., Mayer, B., Shevalier, M., Taylor, S., Nightingale, M., Hutcheon, I., 2009. The use of stable isotope measurements for monitoring and verification of $CO_2$ storage. Energy Procedia 1, 2315–2322. doi:10.1016/j.egypro.2009.01.301.

Keller, J.B., Kolodner, I.I., 1956. Damping of underwater explosion bubble oscillations. Journal of applied physics 27, 1152–1161. doi:10.1063/1.1722221.

Kita, J., Stahl, H., Hayashi, M., Green, T., Watanabe, Y., Widdicombe, S., 2015. Benthic megafauna and $CO_2$ bubble dynamics observed by underwater photography during a controlled sub-seabed release of $CO_2$. International Journal of Greenhouse Gas Control 38, 202–209. doi:10.1016/j.ijggc.2014.11.012.

Kolster, C., Agada, S., Mac Dowell, N., Krevor, S., 2018. The impact of time-varying $CO_2$ injection rate on large scale storage in the UK Bunter Sandstone. International Journal of Greenhouse Gas Control 68, 77–85. doi:10.1016/j.ijggc.2017.10.011.

Leblond, I., Scalabrin, C., Berger, L., 2014. Acoustic monitoring of gas emissions from the seafloor. part i: quantifying the volumetric flow of bubbles. Marine Geophysical Research 35, 191–210. doi:10.1007/s11001-014-9223-y.

Leifer, I., Tang, D., 2007. The acoustic signature of marine seep bubbles. The Journal of the Acoustical Society of America 121, EL35–EL40. doi:10.1121/1.2401227.

Leighton, T., White, P., 2011. Quantification of undersea gas leaks from carbon capture and storage facilities, from pipelines and from methane seeps, by their acoustic emissions. Proceedings of the Royal Society A: Mathematical, Physical and Engineering Sciences 468, 485–510. doi:10.1098/rspa.2011.0221.

Leighton, T.G., 1994. The acoustic bubble. ISBN: 0-12-44190-8 doi:10.1017/S0022112094214519.

Leighton, T.G., Walton, A.J., 1987. An experimental study of the sound emitted from gas bubbles in a liquid. European Journal of Physics 8, 98. doi:10.1088/0143-0807/8/2/005/meta.

Li, J., 2017. DOA tracking in time-varying underwater acoustic communication channels, in: MTS/IEEE OCEANS 2017-Aberdeen, pp. 1–9. doi:10.1109/OCEANSE.2017.8084563.

Li, J., Liao, L., Zakharov, Y.V., 2016. Space-time cluster combining for UWA communications, in: IEEE OCEANS 2016-Shanghai, pp. 1–6. doi:10.1109/OCEANSAP.2016.7485344.

Li, J., Roche, B., Bull, J.M., White, P.R., Davis, J.W., Deponte, M., Gordini, E., Cotterle, D., 2020. Passive acoustic monitoring of a natural $CO_2$ seep site - implications for Carbon Capture and Storage. International Journal of Greenhouse Gas Control 93, 102899 – 102910. doi:10.1016/j.ijggc.2019.102899.

Li, J., White, P.R., B., R., Bull, J.M., W., D.J., Leighton, T.G., Deponte, M., Gordini, E., Cotterle, D., 2019a. Natural seabed gas leakage -- variability imposed by tidal cycles, in: MTS/IEEE OCEANS 2019-Seattle, U.S., pp. 1–6. doi:10.23919/OCEANS40490.2019.8962746.

Li, J., White, P.R., Bull, J.M., Leighton, T.G., 2019b. A noise impact assessment model for passive acoustic measurements of seabed gas fluxes. Ocean Engineering 183, 294–304. doi:10.1016/j.oceaneng.2019.03.046.

Li, J., White, P.R., Roche, B., Bull, J.M., Leighton, T.G., Davis, J.W., Fone, J.W., 2021. Acoustic and optical determination of bubble size distributions - quantification of undersea gas emissions. International Journal of Greenhouse Gas Control , to be presented.

Li, J., White, P.R., Roche, B., Davis, J.W., Leighton, T.G., 2019c. Underwater radiated noise from hydrofoils in coastal water. The Journal of the Acoustical Society of America 146, 3552–3561. doi:10.1121/1.5134779.

Li, J., Zakharov, Y.V., 2018. Efficient use of space-time clustering for underwater acoustic communications. IEEE Journal of Oceanic Engineering 43, 173–183. doi:10.1109/JOE.2017.2688558.

Li, J., Zakharov, Y.V., Henson, B., 2018. Multibranch Autocorrelation Method for Doppler Estimation in Underwater Acoustic Channels. IEEE Journal of Oceanic Engineering 43, 1099 – 1113. doi:10.1109/JOE.2017.2761478.

Liu, J., Chu, N., Qin, S., Wu, D., 2017. Numerical simulations of bubble formation and acoustic characteristics from a submerged orifice: The effects of nozzle wall configurations. Chemical Engineering Research and Design 123, 130–140. doi:10.1016/j.cherd.2017.05.002.

Loewen, M., Melville, W., 1991. A model of the sound generated by breaking waves. J. Acoust. Soc. Am. 90, 2075–2080. doi:10.1121/1.401634.

Mabon, L., Shackley, S., Bower-Bir, N., 2014. Perceptions of sub-seabed carbon dioxide storage in Scotland and implications for policy: a qualitative study. Marine Policy 45, 9–15. doi:10.1016/j.marpol.2013.11.011.

Maggi, A., Duncan, A., 2005. Underwater acoustic propagation modeling software-actup v2. 2l. Centre for Marine Science and Technology, Curtin University, Australia , 1–16.

Murino, V., Regazzoni, C.S., Trucco, A., Vernazza, G., 1994. A noncoherent correlation technique and focused beamforming for ultrasonic underwater imaging: A comparative analysis. IEEE transactions on ultrasonics, ferroelectrics, and frequency control 41, 621–630. doi:10.1109/58.308497.

Nikolovska, A., Sahling, H., Bohrmann, G., 2008. Hydroacoustic methodology for detection, localization, and quantification of gas bubbles rising from the seafloor at gas seeps from the eastern black sea. Geochemistry, Geophysics, Geosystems 9. doi:10.1029/2008GC002118.

Pachauri, R.K., Allen, M.R., Barros, V.R., Broome, J., Cramer, W., Christ, R., Church, J.A., Clarke, L., Dahe, Q., Dasgupta, P., et al., 2014. Climate change 2014: synthesis report. Contribution of Working Groups I, II and III to the fifth assessment report of the Intergovernmental Panel on Climate Change. IPCC.

Pillai, S.U., 2012. Array signal processing. Springer Science & Business Media.

Porter, M.B., 1992. The KRAKEN normal mode program. Technical Report. Naval Research Lab Washington DC.

Roberts, J.J., Gilfillan, S.M., Stalker, L., Naylor, M., 2017. Geochemical tracers for monitoring offshore $CO_2$ stores. International Journal of Greenhouse Gas Control 65, 218–234. doi:10.1016/j.ijggc.2017.07.021.

Roelofse, C., Alves, T.M., Gafeira, J., Kamal'deen, O.O., 2019. An integrated geological and GIS-based method to assess caprock risk in mature basins proposed for carbon capture and storage. International Journal of Greenhouse Gas Control 80, 103–122. doi:10.1016/j.ijggc.2018.11.007.

Schmidt, R., 1979. Multiple emitter location and signal parameter estimation, in: Proc. RADC Spectrum Estimation Workshop, Washington, IEEE. pp. 1243–258. doi:10.1109/TAP.1986.1143830.

Schmidt, R., 1986. Multiple emitter location and signal parameter estimation. IEEE transactions on antennas and propagation 34, 276–280. doi:10.1109/TAP.1986.1143830.

Shell, 2017. Goldeneye Gas Platform, United Kingdom. URL: http://www.offshore-technology.com/projects/goldeneye/.

Shitashima, K., Maeda, Y., Sakamoto, A., 2015. Detection and monitoring of leaked $CO_2$ through sediment, water column and atmosphere in a sub-seabed CCS experiment. International Journal of Greenhouse Gas Control 38, 135–142. doi:10.1016/j.ijggc.2014.12.011.

Somasundaram, S., 2011. Reduced dimension robust capon beamforming for large aperture passive sonar arrays. IET radar, sonar & navigation 5, 707–715. doi:10.1049/iet-rsn.2010.0351.

Speiser, J.M., 1986. Progress in eigenvector beamforming, in: Real-Time Signal Processing VIII, International Society for Optics and Photonics. pp. 2–8. doi:10.1117/12.949696.

Stalker, L., Noble, R., Pejcic, B., Leybourne, M., Hortle, A., Michael, K., Dixon, T., Basava-Reddi, L., 2012. Feasibility of monitoring techniques for substances mobilised by $CO_2$ storage in geological formations. Energy Procedia 23, 439–448. doi:10.1016/j.egypro.2012.06.039.

Stork, A.L., Allmark, C., Curtis, A., Kendall, J.M., White, D.J., 2018. Assessing the potential to use repeated ambient noise seismic tomography to detect $CO_2$ leaks: Application to the Aquistore storage site. International Journal of Greenhouse Gas Control 71, 20–35. doi:10.1016/j.ijggc.2018.02.007.

Strachan, N., Hoefnagels, R., Ramírez, A., Van den Broek, M., Fidje, A., Espegren, K., Seljom, P., Blesl, M., Kober, T., Grohnheit, P.E., 2011. CCS in the North Sea region: A comparison on the cost-effectiveness of storing $CO_2$ in the Utsira formation at regional and national scales. International Journal of Greenhouse Gas Control 5, 1517–1532. doi:10.1016/j.ijggc.2011.08.009.

Sutton, J.L., 1979. Underwater acoustic imaging. Proceedings of the IEEE 67, 554–566. doi:10.1109/PROC.1979.11283.

Szulejko, J.E., Kumar, P., Deep, A., Kim, K.H., 2017. Global warming projections to 2100 using simple $co_2$ greenhouse gas modeling and comments on $co_2$ climate sensitivity factor. Atmospheric Pollution Research 8, 136–140. doi:10.1016/j.apr.2016.08.002.

Tappert, F.D., 1977. The parabolic approximation method, in: Wave propagation and underwater acoustics. Springer, pp. 224–287. doi:10.1007/3-540-08527-0_5.

Taylor, P., Stahl, H., Vardy, M.E., Bull, J.M., Akhurst, M., Hauton, C., James, R.H., Lichtschlag, A., Long, D., Aleynik, D., et al., 2015. A novel sub-seabed $CO_2$ release experiment informing monitoring and impact assessment for geological carbon storage. International Journal of Greenhouse Gas Control 38, 3–17. doi:10.1016/j.ijggc.2014.09.007.

Van Veen, B.D., Buckley, K.M., 1988. Beamforming: A versatile approach to spatial filtering. IEEE ASSP magazine 5, 4–24. doi:10.1109/53.665.

Vielstädte, L., Linke, P., Schmidt, M., Sommer, S., Haeckel, M., Braack, M., Wallmann, K., 2019. Footprint and detectability of a well leaking $CO_2$ in the Central North Sea: Implications from a field experiment and numerical modelling. International Journal of Greenhouse Gas Control 84, 190–203. doi:10.1016/j.ijggc.2019.03.012.

Wan, S., Zhao, Y., Wang, T., Gu, Z., Abbasi, Q.H., Choo, K.K.R., 2019. Multi-dimensional data indexing and range query processing via Voronoi diagram for internet of things. Future Generation Computer Systems 91, 382–391. doi:10.1016/j.future.2018.08.007.

599 Yap, C.K., 1987. AnO (n logn) algorithm for the voronoi diagram of a set of simple curve segments. Discrete
600 & Computational Geometry 2, 365–393. doi:10.1007/BF02187890.

601 Zoback, M.D., Gorelick, S.M., 2012. Earthquake triggering and large-scale geologic storage of carbon dioxide.
602 Proceedings of the National Academy of Sciences 109, 10164–10168. doi:10.1073/pnas.1202473109.